Novel Actuation Techniques for Piezoelectric Tube Actuators

Dissertation

Precision Mechatronics Lab

Digvijay Singh Raghuvanshi

October 26, 2018

Supervisors

A/Prof Yuen K Yong

Prof Andrew J Fleming

Dr Steven I Moore

A thesis submitted in fulfilment of the requirements for the degree of Master of Philosophy in Electrical Engineering at The University of Newcastle, Australia.

Statement of originality

I hereby certify that the work embodied in the thesis is my own work, conducted under normal supervision.

The thesis contains no material which has been accepted, or is being examined, for the award of any other degree or diploma in any university or other tertiary institution and, to the best of my knowledge and belief, contains no material previously published or written by another person, except where due reference has been made in the text. I give consent to the final version of my thesis being made available worldwide when deposited in the University's Digital Repository, subject to the provisions of the Copyright Act 1968 and any approved .

Digvijay Singh Raghuvanshi, October 26, 2018

Statement of collaboration

I hereby certify that the work embodied in this thesis has been done in collaboration with other researchers and staff at the University of Newcastle. I have included as part of the thesis a statement clearly outlining the extent of collaboration, with whom and under what auspices.

- In Section 3.4 and Section 4.4, the experiment jigs were prepared in collaboration with Mr. Phillip Dombkins and Mr. Peter Turner from the machining shop.
- In Section 3.4 and Section 4.4, the preparation of electrodes on the tubes was conducted in collaboration with Mr. Ben Routley from Precision Mechatronics Lab.
- In Section 4.2, the analytical modelling for an eight-electrode tube was conducted in collaboration with Dr. Steven I. Moore from Precision Mechatronics Lab.

Digvijay Singh Raghuvanshi, October 26, 2018

Acknowledgment

I expresses my most sincere gratitude and personal homage to my supervisors Dr. Yuen K. Yong and Dr. Andrew J. Fleming for giving me the opportunity to undertake this project at a state-of-the-art facility, the Precision Mechatronics Lab. I am grateful for their invaluable guidance and support throughout the research and to my fellow lab members Mr. Meysam Omidbeike and Mr. Ben Routley for their time and support during experiments. A very special thanks to Dr. Steven I. Moore for providing valuable insights during the analytical modelling and being a mentor while compiling thesis results with constant words of motivation. I thank Mr. Phillip Dombkins and Mr. Peter Turner from the machining shop for their assistance in experimental setup. A sincere thanks to the PVC Office, the School Office and the Graduate Studies Office for the administrative support during my RHD tenure. A very warm thanks to all the office colleagues of EF-108 room in Engineering F building for uplifting my spirits through tough days. Most above, I am forever grateful to my parents and mentors Dr. Shashee K. Raghuvanshi and Mrs. Rita Raghuvanshi for being the pillars of personal support, and to the love of my life and my best friend, Mahima, for believing in me and waiting for me. I am grateful to the entire University of Newcastle for giving an international student the opportunity, the environment and the support to carry out an engineering research, allowing a small town boy across the seas to take the first step towards his goals.

OM NAMAH SHIVAYA

(glory to Shiva, the transformer, the destroyer, the supreme reality, the inner self, the consciousness that dwells in all)

Abstract

Piezoelectric tube actuators are widely used in applications such as fibre optics alignment, endoscopy imaging and scanning probe microscopy. Piezoelectric tubes are thin-walled cylinders of radially poled piezoelectric ceramics. In almost all applications, the tube is fixed at one end and free at the other. A conventional tube in atomic force microscopy consists of quartered outer electrodes, which cover two-thirds of the length for lateral actuation. The remaining one-third of the length is covered by a circumferential electrode for vertical actuation. The inner surface is covered by a continuous electrode grounded at all times. For lateral actuation (bending) along the X or Y-direction, two outer quartered electrodes on opposite sides are driven by voltages of equal magnitude but opposite polarity. Voltage applied to the top circumferential electrode produces vertical actuation.

The simplest way to increase the scan range of a piezoelectric tube actuator is to increase its length. However, this increases the physical size and reduces the resonance frequency. This thesis describes a new method for increasing the vertical scan range by driving the internal electrode rather than grounding it. This approach eliminates the need for a circumferential Z-electrode, which is typically one-third of the tube length, thereby allowing longer quadrant electrodes for larger lateral scan range. Since the proposed technique does not change the physical size of the tube, it is ideal for compact applications. Experimental results show a 62% increase in lateral scan range and an 86% increase in vertical scan range with negligible increase in cross-coupling. Analytical modelling shows that driving the internal electrode does not interfere with the lateral scan range.

This thesis also proposes to implement similar technique for an eight-electrode tube actuator to compensate for angular (tilting) and vertical cross-coupling. The conventional quartered electrodes are split into two vertical segments of equal length to create a total of eight electrodes. The tilting and vertical cross-coupling due to the lower segments is compensated by the upper segments giving a sigmoid shape to the tube during lateral motion. Finite element simulations and experimental results confirm a 96% decrease in tilt angle and 43% reduction in vertical cross-coupling. However, the trade-off encountered with this method is a 44% decrease in lateral scan range.

Publications

- Digvijay S. Raghuvanshi, Steven I. Moore, Andrew J. Fleming and Yuen K. Yong, "Electrode Configurations for Piezoelectric Tube Actuators with Improved Scan Range and Reduced Cross-Coupling", IEEE/ASME Trans. Mechatronics (under review).

Contents

List of Figures

List of Tables

Chapter 1

Introduction

1.1 Outline of Thesis

This thesis consists of five chapters. An overview of the contents is shown in Table 1.1.

Table 1.1: Outline of thesis.

Chapter	Descriptions/Aims	Contributions
1	Introduction	A review of piezoelectricity, applications and conventional design of piezoelectric tube actuator. The chapter outlines the research contributions by the thesis.
2	Understanding the conventional design and its significance.	Finite-element analysis of deflection and tilt angle on varying the electrode length.
3	To increase scan ranges of conventional piezoelectric tube actuators.	Complete description and comparison of designs, analytical estimations, FE models, and experimental results of the conventional and proposed techniques.
4	To reduce tilt angle, vertical cross-coupling and increase the vertical scan range of piezoelectric tube actuators.	Complete description and comparison of designs, analytical estimations, FE models, and experimental results of the conventional and proposed techniques.
5	Conclusions and future work.	Summarizing results and future directions.

1.2 Introduction of Piezoelectricity

The piezoelectric effect relates mechanical stress to electric charge within a class of crystalline materials [2]. These materials have a crystalline lattice which deforms under the influence of an external force to create a dipole moment due to the separation and alignment of positive and negative charges [3]. Such a dipole induces an electric charge which is measurable on the material surface. This property is referred to as the direct piezoelectric effect. When operating in this mode, the material is being used as a sensor. Conversely, the crystalline lattice experiences mechanical strain when an electric field is applied across the material thickness causing measurable structural deformation. This property is referred to as the inverse piezoelectric effect. The direction of deformation or strain can be reversed if the polarity of the

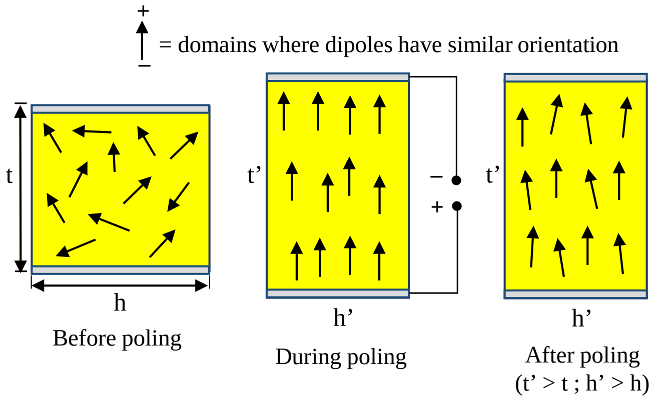

Figure 1.1: Polling process of a piezoelectric ceramic [1].

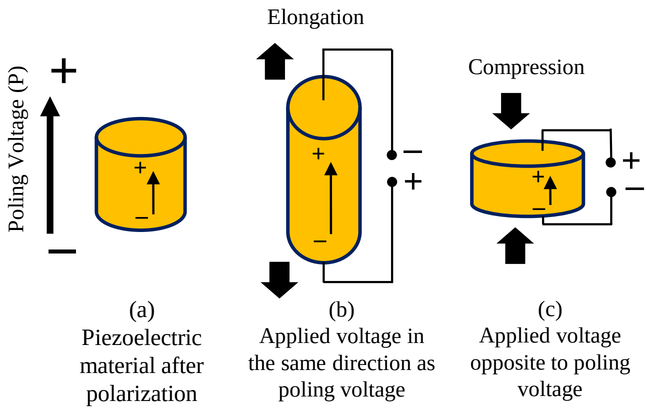

Figure 1.2: Elongation and compression of a piezoelectric material corresponding to the voltage polarity.

applied electric field is reversed. When operating in this mode, the material is being used as an actuator.

The piezoelectric effect is naturally occurring in monocrystalline piezoelectric materials such as quartz and tourmaline, however, is insufficient for high-end solid state sensing-actuation applications. Industrial poling processes were introduced in 1960s to create man-made polycrystalline piezoelectric ceramics such as barium titanate ($BaTiO_3$) from metallic oxides and lead-zirconate-titanate (PZT) materials. PZT materials exhibit larger sensitivity and higher Curie temperatures compared to $BaTiO_3$ and have since been the most widely used ceramics for solid state sensing-actuation applications [4, 5]. These ceramics have much higher polarization within their lattice resulting in an efficient conversion of electrical energy to mechanical strain and vice versa. The piezoelectric tube actuator discussed in this thesis is made from PZT-5H ceramic.

Before poling, the piezoelectric ceramic consist of randomly oriented domains as shown in Fig.1.1. The material produces no net effect when a mechanical stress or an electric field is applied [1]. The poling process enables the piezoelectric effect by heating the material near its Curie temperature (typically between 100°C and 300°C), followed by the application of a strong electric field [1]. As the field is maintained during cooling, the dipoles align with the field and a majority of them maintain their alignment. The dimensions of the ceramic is changed permanently after poling as shown in Figure 1.1. The poling axis is the direction between the poling electrodes. As described in Figure 1.2, if a voltage of the same polarity as the poling voltage is applied to the ceramic (in the direction of the poling voltage),

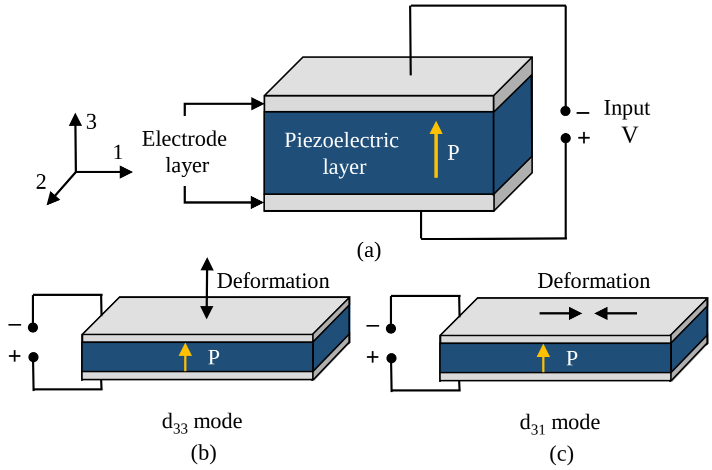

Figure 1.3: (a) Schematic of a piezoelectric material with its polarization (P) direction. Deformation of the material in d_{33} mode (b) and d_{31} mode (c).

the ceramic will extend and its diameter will contract due to the Poisson effect. If applying a voltage of polarity opposite to that of the poling voltage, the ceramic will contract and its diameter will increase.

Considering voltage is applied across the material thickness as shown in Figure 1.3, the constitutive equations of a transducer made of a one-dimensional piezoelectric material can be expressed as [6–8]

$$S_1 = s_{11}^E T_1 + d_{31} E_3, \tag{1.1}$$

$$D_3 = d_{31} T_1 + \varepsilon_{33}^T E_3, \tag{1.2}$$

where S_1 is the mechanical strain (in m/m), T_1 is the mechanical stress (in N/m^2), s_{11} is the compliance of Young's modulus, d_{31} is piezoelectric constant (in C/N), D_3 is the electric displacement (in C/m^2), E_3 is the electric field (in V/m), and ε_{33} is the permittivity (F/m). The superscripts E and T represent measurements taken under constant electric field and constant stress respectively. The subscripts refer to different directions within the material coordinate system as shown in Figure 1.3. d_{31} refers to the case when the electric field is applied along the poling direction (3-direction) but produces mechanical strain perpendicular to the poling direction, which is along the 1-direction. Due to the Poisson effect, d_{31} is usually a negative number. The above equations can be written alternatively as

$$T_1 = c_{11}^E S_1 - e_{31} E_3, \tag{1.3}$$

$$D_3 = e_{31} S_1 + \varepsilon_{33}^S E_3, \tag{1.4}$$

where $c_{11} = 1/s_{11}$ is the Young's modulus (in N/m^2), e_{31} is the piezoelectric constant (in C/m^2). The superscript S represents measurements taken under constant strain. Equation (1.3) and (1.4) will be used to analyse the deflections of piezoelectric tube actuators in Chapters 3 and 4.

1.3 Applications of Piezoelectric Actuators

A piezoelectric actuator converts an applied electrical input/signal into useful mechanical output in the form of physical deformation (strain) based on the principle of inverse piezoelectric effect. The common forms of piezoelectric actuators include benders [9–12], stacks [13–15], and piezoelectric tube actuators [16]. The fine resolution of piezoelectric materials has enabled their use in a variety of actuation

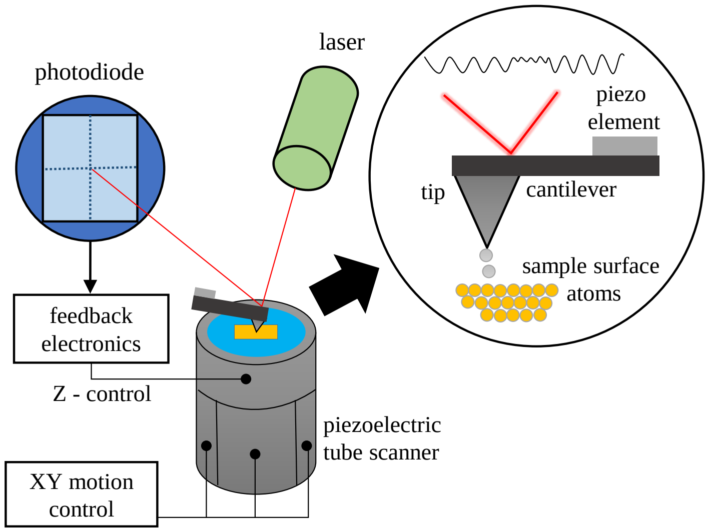

Figure 1.4: A piezoelectric tube actuator is used as a XYZ scanner in Atomic Force Microscopy.

applications which require sensitivity and precision [17, 18]. These applications include atomic force microscopy [19], flexure-based nanopositioners [20–23], medical devices [24], and fuel injection control valves in automobiles [25].

Since the inception of scanning tunnelling microscope (STM) by Binnig et al. [26], it has been a fundamental tool for the study, analysis, and manipulation of matter at nanoscale. Binnig and co-workers developed an atomic-resolution 3D image of a conducting surface by using a close-proximity tunnelling current between a sharp probe tip and a conducting surface [27]. In the early development, STMs used tripod scanners with piezoelectric stack actuators forming a tripod stand [26]. A sharp probe was located at the meeting junction of the three tripod legs. Actuating a combination of these stack actuators facilitated XYZ motions of the probe. However, the tripod scanner is bulky [26] and rarely used in modern STMs. Binnig and Smith were the first to introduce a piezoelectric tube actuator with quartered electrodes for XYZ positioning in STM [27]. Since then, many commercial STMs use piezoelectric tube actuators for 3D positioning of the tunnelling probe.

Piezoelectric tube actuators have also become the commonly used XYZ scanners in Atomic Force Microscopy (AFM) due to their simple mechanical structure, relatively low cost, and ease of installation [21, 28, 29]. The atomic force microscope (AFM), also invented by Binnig and co-workers [30], is one of the most versatile tools in imaging structures on an atomic scale. AFMs can be operated in air, vacuum and fluid. They can be used to interrogate both conductive and non-conductive materials. A piezoelectric tube actuator is used to precisely move a sample into contact with a sharp probe (located at the free-end of a cantilever) as shown in Figure 1.4. The cantilever deflects towards or away from the sample due to close-range inter atomic forces between the probe and sample. These deflections can be detected accurately by using a laser and a position-sensitive photodiode. A 3D topography image of the material surface can therefore be constructed by scanning the cantilever over a sample region. Typically the Z-axis of the scanner is controlled to keep the deflection of the cantilever constant and by plotting the Z-axis control action as a function of the XY position of the scanner the topography image is formed.

The applications of AFM have extended to nanofabrication and nano-patterning [31–35]. In nano-patterning applications, the piezoelectric tube actuator is used to position a probe to deposit or remove nanoparticles from a sample. Piezoelectric tube actuators have also been used in micro-contact printing to generate patterns on organic surfaces [33]. Other precision applications include fiber optic interfer-

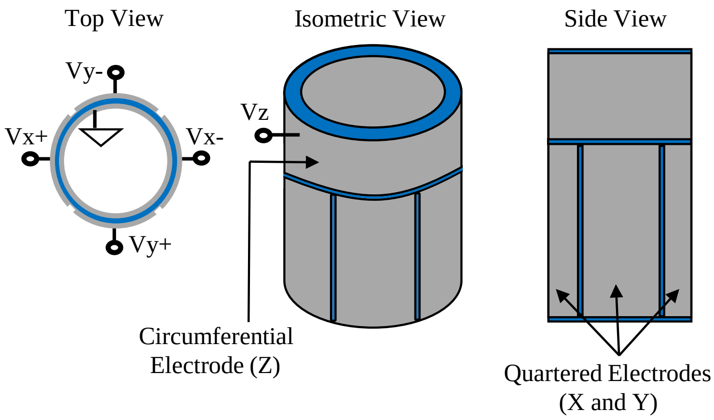

Figure 1.5: Schematic of a conventional piezoelectric tube.

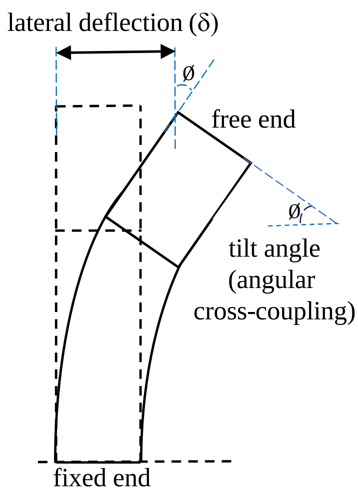

Figure 1.6: Schematic showing initial and final positions of a conventional piezoelectric tube during bending. Cross-coupling in the form of tilt angle is shown. Displacements are exaggerated for clarity.

ometry [36] and endoscopic imaging [37]. In endoscopic optical coherence tomography (OCT), the tube positions an optical fibre/endoscope probe which is mostly linked with a catheter and is sent into a specimen to acquire 3D OCT images [38, 39].

1.4 Limitations of Piezoelectric Tube Actuators

The piezoelectric tube actuator is a thin-walled hollow cylinder made of radially poled piezoelectric ceramic. The conventional actuation method [40, 41] uses four external quartered electrodes and a single circumferential Z-electrode to generate three degrees-of-freedom (DOF) motion as shown in Figure 1.5. The internal electrode is grounded. One end of the tube is fixed and the other end is free. The tube undergoes physical deformation when an electric field is applied across its material due to the inverse piezoelectric effect to produce radial, lateral or axial displacements. An electric field applied in the direction of poling voltage (radially) will extend the tube thickness causing axial contraction in the orthogonal direction. Conversely an electric field applied opposite to the poling voltage will cause extension in the orthogonal direction. Therefore, when voltages with equal magnitude but opposite polarity are applied

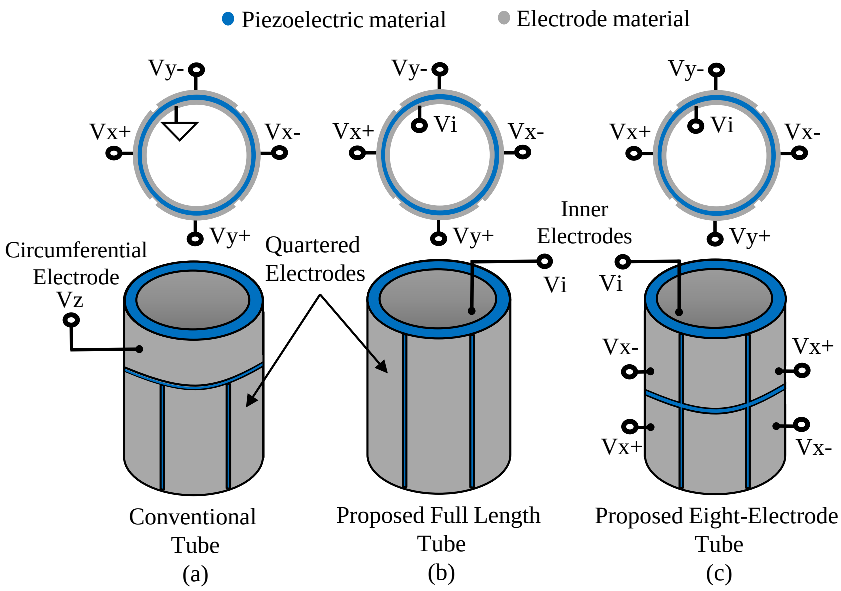

Figure 1.7: Electrode design and drive configuration of the (a) conventional actuation technique, (b) proposed full-length actuation technique, and (c) proposed eight-electrode actuation technique.

to a pair of opposite quartered electrodes, one side of the tube extends while the opposite side contracts, resulting in bending as shown in Figure 1.6. Similarly, the other pair of electrodes provide actuation in the orthogonal direction. To displace in the Z direction, voltage is applied to the circumferential Z-electrode which is conventionally one-third of the tube length and located at the free-end of the tube.

One limitation of the piezoelectric tube actuator is that the Z-deflection is small, typically in the range of 1 μm to 3 μm [42]. Scanning in X- or Y- (lateral) direction produces motion of any given sample point on a convex-like surface which results in varying Z-displacements of the sample point. When the piezoelectric tube is scanned over a large area on the XY-plane, the Z-displacement may go beyond the vertical compensation limits of the piezoelectric tube. This results in imaging errors and distortions.

Another limitation is that the lateral bending of the piezoelectric tube actuator follows an angular trajectory due to the fixed-free boundary condition. This results in an inherent vertical cross-coupling, and an angular cross-coupling (tilting) that causes the moving platform to tilt from its original horizontal plane. Providing that the tube has sufficient Z-displacement range, feedback or feedforward techniques can be implemented to compensate for the vertical cross-coupling [43]. However, the tilting remains an issue.

1.5 Contributions of the Research

1.5.1 Increasing the vertical and lateral scan range

The simplest way to increase the bending (lateral motion) of a piezoelectric tube is to increase its length. However, this increases the physical size and cost of the tube. This thesis proposes a new method for increasing the vertical scan range of piezoelectric tube actuators by driving the internal electrode rather than grounding it, as described in Figure 1.7(b). This approach eliminates the need for a circumferential Z-electrode, which is typically one-third of the tube length, thereby allowing longer quadrant electrodes for larger lateral scan range. Since the proposed technique does not change the physical size of the tube, the proposed method is ideal for compact applications. A comparative analysis of the conventional and proposed actuation techniques have been conducted through finite-element analysis (FEA) on the two tube models and verified through experiments on PZT-5H material, discussed in Chapter 3. Experiment results show a 62% increase in lateral scan range and an 86% increase in vertical scan range.

1.5.2 Simultaneously increasing the vertical scan range and reducing tilting and vertical cross-coupling

In Chapter 4, the thesis proposes a new electrical configuration for piezoelectric tube actuators which eliminates the tilting and vertical cross-coupling at the moving end, and significantly increases the vertical scan range, as described in Figure 1.7(c). The proposed configuration includes a driven internal electrode for vertical motion, and eight external electrodes for lateral motion. Lower half of the tube is used to create bending, while the upper half corrects for tilting and vertical cross-coupling. Experimental results demonstrate a 44% increase in vertical displacement, a 96% reduction in tilting, and 43% reduction in vertical cross-coupling compared to the conventional tube.

Chapter 2

Quantitative Analysis of Varying Electrode Length

2.1 Introduction

The piezoelectric tube actuator has a fixed-free boundary condition. Lateral deflections are generated at the free-end of the tube when the quartered electrodes are actuated. During bending, the angular motion of the tube causes the moving platform to tilt from its original horizontal plane. The tilt angle distorts interference pattern in optical microscopy [44] and reduces image quality in atomic force microscopy [42].

Conventionally, two-third of the piezoelectric tube actuator length is covered by quartered electrodes for lateral actuation and one-third of the length is covered by a single circumferential Z-electrode for vertical actuation. Although many commercial piezoelectric tube actuators have used the same ratio, the advantage is not justified. There is no quantitative analysis in the literatures reporting the trade-off between the length of quartered electrodes versus lateral deflection and tilt angle. This chapter investigates the impact of electrode length on the lateral deflection and tilting by modeling the piezoelectric tube actuator using a commercial finite-element (FE) package ANSYS.

The FE results on lateral deflection have been compared with the widely used equation in [45]. The nominal difference between the FE simulated results and that of [45] is within 15%.

2.2 Finite-Element-Analysis

A piezoelectric tube actuator which is made of PZT-5H piezoelectric ceramic material having length 50.8 mm, thickness 0.66 mm and outer diameter 9.5 mm is used in this study. As illustrated in Figure 2.1(a), ten piezoelectric tube actuators with a uniformly increasing quartered-electrode length are modelled using ANSYS workbench. An aluminium platform is also modelled in order to simulate the tilt angle. The length of the quartered electrodes are gradually increased from 10% to 100% of the total tube length, and the defection (δ_x) and tilt angle (ϕ) are recorded. ANSYS PiezoAndMEMS Application Customization Toolkit extension is used to model the piezoelectric property of the tube with piezoelectric coefficients in stress form (e), the relatively permittivity ϵ^S/ϵ_o and the piezoelectric constant d_{31}, as shown in Table 2.1. A cylindrical coordinate system is used to define the polarization vector of the tube which is radially inwards. Voltages are applied to the X-electrodes to simulate maximum deflection (δ_x) and tilt angle (ϕ) as shown in Figure 2.1(b). Y-electrodes and the inner surface are grounded in the model.

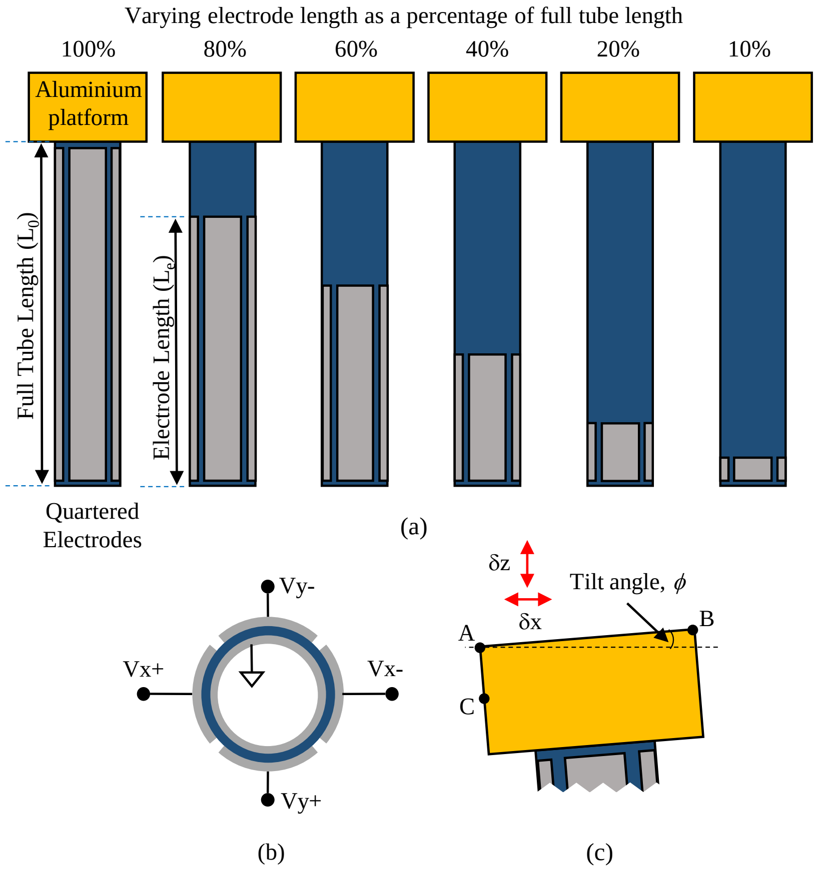

Figure 2.1: (a) A piezoelectric tube actuator model with varying electrode length. (b) Actuation configuration is shown. (c) Deflection δ_x and tilt angle ϕ is shown. Locations of nodes where deformations are recorded in ANSYS.

Parameters of the tube are described in Table 2.2. The lateral deflection δ_x is recorded at point E as shown in Figure 2.1(c). L_e is the length of the quartered electrodes, and L_o is the total length of the tube actuator. Point C is the location of a sensor used to measure the lateral deflection of the piezoelectric tube actuator in experiments, which is discussed in Chapter 3 and 4. δ_{z_A} and δ_{z_B} are the vertical displacements at points A and B as shown in Figure 2.1(c). l_{AB} is the length of the edge AB of the aluminium platform. The percentages of reduction in δ_x and ϕ, denoted as $P_{\delta x}$ and P_ϕ respectively, are estimated with respect to their maximum values at $L_e = L_o$ as described in Table 2.2.

2.3 Results and Comparisons

Percentages of reduction in δ_x and ϕ with varying the electrode length L_e are compared in Table 2.3. Figure 2.2(a) plots the percentages of reduction, $P_{\delta x}$ and P_ϕ, versus the percentage of reduction in L_e. P_ϕ is linearly proportional to the percentage of reduction of L_e, however, $P_{\delta x}$ exhibits a nonlinear relationship. Ideally, the piezoelectric tube actuator should have a maximum lateral deflection with a minimum tilt angle. To search for a trade-off region, P_ϕ versus $P_{\delta x}$ is plotted in Figure 2.2(b). There exists a region where the reduction in ϕ is within 20% to 40% without compromising the lateral deflection significantly (that is within 8.4% to 22.6% reduction in δ_x). This region is highlighted in Table 2.3.

Table 2.1: Piezoelectric properties of the tube actuators.

Piezoelectric coefficient, C/m^2	
e_{31}	-6.55
e_{33}	23.3
Relative permittivity, ϵ^S/ϵ_o	
ϵ_{11}	1700
ϵ_{33}	1470
Piezoelectric constant, $\times 10^{-12}$m/V	
d_{31}	-274

Table 2.2: Tube parameters and notations.

Descriptions	Parameters and Calculations
Electrode length	L_e
Total tube length	L_o
Maximum lateral deflection when L_e = L_o	δ_{xo}
Maximum tilt angle when L_e = L_o	ϕ_o
Lateral deflection	δ_x
Tilt angle	$\phi = (\delta_{z_A} - \delta_{z_B})/l_{AB}$
Percentage of reduction in δ_x	$P_{\delta x} = (\delta_{xo} - \delta_x)/\delta_{xo} \times 100$
Percentage of reduction in ϕ	$P_\phi = (\phi_o - \phi)/\phi_o \times 100$

Table 2.3: Percentage of reduction in deflection and tilt angle with varying quartered-electrode length.

Sample No.	L_e (mm)	% of active L_o $L_e/L_o \times 100$	% Reduction in L_e	% Reduction in δ_x $P_{\delta x}$	% Reduction in ϕ P_ϕ
0	0	0	100	100	100
1	5.08	10	90	83	89.7
2	10.16	20	80	68	79.8
3	15.24	30	70	54.6	69.8
4	20.32	40	60	42.5	59.9
5	25.4	50	50	31.8	49.9
6	30.48	60	40	22.6	40
7	35.56	70	30	14.8	30
8	40.64	80	20	8.4	20.2
9	45.72	90	10	3.4	10.2
10	50.8	100	0	0	0

The conventional piezoelectric tube actuators fall within this region [40,41]

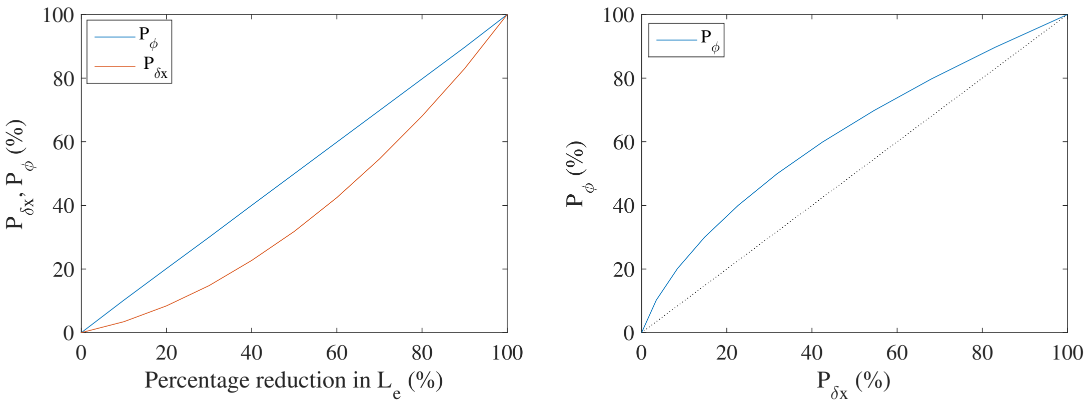

(a) (b)

Figure 2.2: FE simulated results. (a) Percentage of reduction in δ_x (denoted by $P_{\delta x}$) and ϕ (denoted by P_ϕ) with respect to that in L_e. (b) Percentage of reduction in ϕ with respect to that in δ_x.

Chapter 3

A Novel Actuation Technique for Piezoelectric Tube Actuators

3.1 Introduction

This chapter compares the conventional piezoelectric tube actuation technique [40,41] with a new actuation approach as described in Figure 3.1. The proposed method achieves vertical actuation by driving the internal electrode with a negative voltage rather than connecting it to ground. The use of an inner electrode eliminates the need for a circumferential Z-electrode, thereby allowing longer quadrant electrodes and increased lateral displacement. To avoid generating an electric field opposite to the polarization vector, the internal voltage is restricted to a negative polarity. This is a conservative choice that avoids the possibility of exceeding the coercive field strength of the piezoelectric material. It should be noted that the maximum electric field in the poling direction is doubled by the proposed method; however, this is typically five times the coercive field strength, so the resulting electric field is less than half of the limiting value. It is analytically deduced that driving the internal electrode does not affect lateral scan range. Experimental results show a 62% increase in lateral scan range and an 86% increase in the vertical scan range.

3.2 Analytical Estimations of Deflections

This section derives the tube deflection based on the Euler-Bernoulli equations. To produce lateral deflection along the Y-axis, the Y-electrodes are driven differentially with $\pm V_y$ volts as shown in Figure 3.2. The X-electrodes are grounded and the internal electrode is actuated with V_i volts. Lateral deflection along the X-axis can be derived similarly by applying differential voltages to the X-electrodes. The transformation $(x, y) = (-rcos\theta, -rsin\theta)$ converts cartesian coordinates to cylindrical coordinates. Tube is considered thin with radius r. In the polar coordinate, the applied voltage $V(\theta)$ is,

$$V(\theta) = \begin{cases} -V_y - V_i & \theta \in (\pi/4, 3\pi/4), \\ V_y - V_i & \theta \in (5\pi/4, 7\pi/4), \\ 0 & \text{otherwise.} \end{cases} . \tag{3.1}$$

Applying Euler-Bernoulli kinematic assumptions [46], the strain S_1 is

$$S_1(z, r, \theta) = -yw_0''(z) = r\sin(\theta)w_0''(z), \tag{3.2}$$

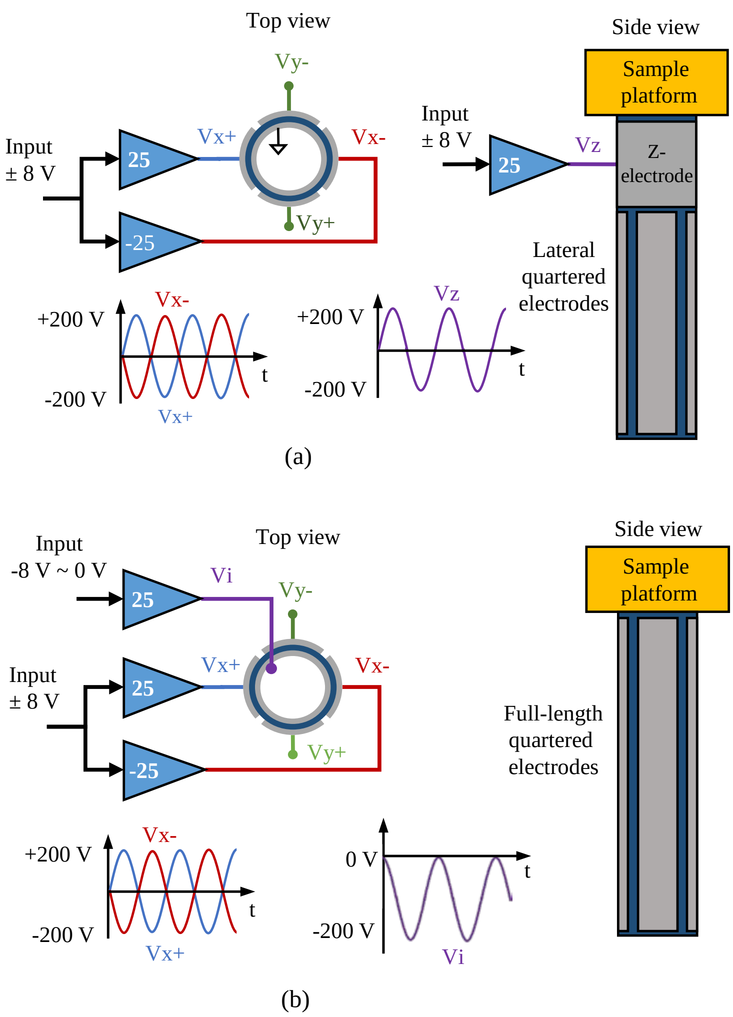

Figure 3.1: Electrode configuration and driving method for the (a) conventional and (b) proposed piezoelectric tube actuator.

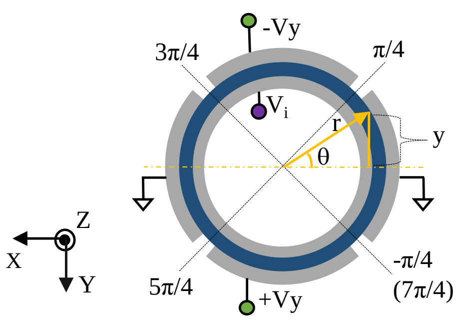

Figure 3.2: A cross-section of the tube in the XY plane. The Y-electrodes are driven with equal but opposite voltages V_y, and the internal electrode is driven by V_i. The X-electrodes are grounded.

where (z, r, θ) are cylindrical co-ordinates and $w_0(z)$ is the lateral deflection as a function of z across the length of the tube. In the Euler-Bernoulli beam, all other strains are zero. The constitutive equations [7,8] of the piezoelectric material (Equations (1.3) and (1.4)) are

$$T_1 = ES_1 - e_{31}E_3, \tag{3.3}$$
$$D_3 = e_{31}S_1 + \varepsilon_{33}^S E_3, \tag{3.4}$$

where T_1 is the stress, E is the elastic modulus, e_{31} is the piezoelectric coefficient, E_3 is the electric field, D_3 is the electric displacement, and ε_{33}^S is the permittivity. Assuming a thin tube structure, the electric field is a function of voltage given by

$$E_3 = V(\theta)/h, \tag{3.5}$$

where h is the thickness of the tube. Substituting (3.2) and (3.5) into (3.3) results in the following expression for the stress around the circumference of the tube,

$$T_1 = Er\sin(\theta)w_0''(z) - e_{31}V(\theta)/h. \tag{3.6}$$

The first part of this expression is the stress caused by the mechanical structure and the second part is the stress due to the piezoelectric effect. These stresses induce moments which cause the cross-sectional area to rotate around the neutral axis. Assuming there is no net axial force on the structure, the total moment on the cross-sectional area is

$$M = \int_0^{2\pi} yT_1 d\theta. \tag{3.7}$$

From Figure 3.2, $y = -r\sin(\theta)$, therefore,

$$\begin{aligned}
M &= \int_0^{2\pi} -r\sin(\theta)T_1 d\theta, && (3.8)\\
&= -\int_{-\pi/4}^{\pi/4} Er^2\sin^2(\theta)w_0''(z)d\theta \\
&\quad -\int_{\pi/4}^{3\pi/4} [Er^2\sin^2(\theta)w_0''(z) - e_{31}rsin(\theta)\frac{(-V-V_i)}{h}]d\theta \\
&\quad -\int_{3pi/4}^{5\pi/4} Er^2\sin^2(\theta)w_0''(z)d\theta \\
&\quad -\int_{5pi/4}^{7\pi/4} [Er^2\sin^2(\theta)w_0''(z) - e_{31}rsin(\theta)\frac{(V-V_i)}{h}]d\theta, \\
&= -Er^2w_0''(z)\pi + \frac{\sqrt{2}e_{31}r}{h}(-V-V_i-V+V_i), && (3.9)\\
&= -Er^2w_0''(z)\pi - \frac{2\sqrt{2}e_{31}rV}{h}. && (3.10)
\end{aligned}$$

Note that the voltage of the inner electrode (V_i) is eliminated in the above expression, indicating the internal driving voltage has no effect on the lateral deflection of the tube. With no external load, the net moment is zero when in equilibrium, that is,

$$M = -Er^2w_0''(z)\pi - \frac{2\sqrt{2}e_{31}rV_y}{h} = 0. \tag{3.11}$$

Rearranging the above equation and substituting $r = D/2$ and $e_{31} = Ed_{31}$ gives

$$w_0''(z) = -\frac{4\sqrt{2}d_{31}V_y}{hD\pi}, \tag{3.12}$$

where, d_{31} is the piezoelectric strain constant and D is the tube diameter. To obtain an expression for the lateral deflection, double integration is performed on (3.12) with the boundary conditions $w'(z) = 0$ at $z = 0$, and $w_0(z) = 0$ at $z = 0$. The deflection of the tube at $z = L$ is

$$w_0(L) = \delta_y = -\frac{2\sqrt{2}d_{31}L^2V_y}{\pi Dh}, \tag{3.13}$$

which is identical to that derived by Chen [45]. For vertical motion, the standard deflection equation is used,

$$\delta_z = -\frac{d_{31}LV_i}{h}, V_i < 0. \tag{3.14}$$

3.3 Finite-Element-Analysis

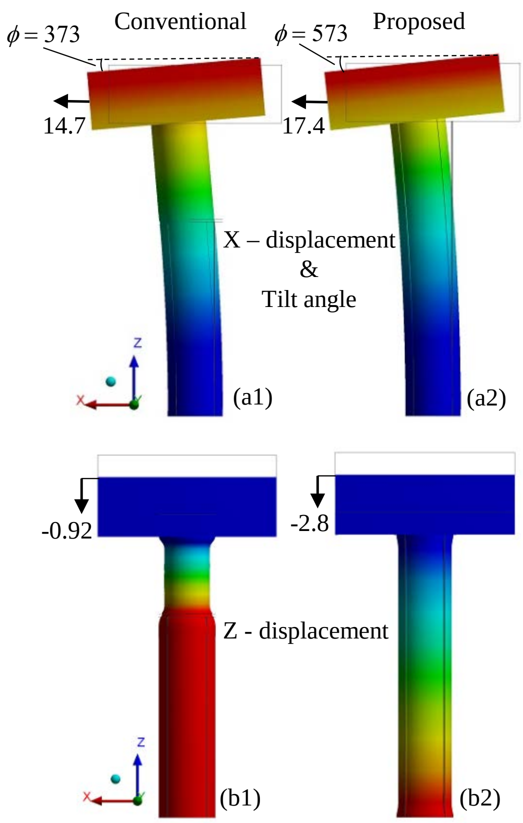

Figure 3.3: (a) FE simulated deflection (in μm) and tilt angle (in μrad) of the conventional (a1 & b1) and proposed (a2 & b2) piezoelectric tube actuators. Displacements are exaggerated for clarity.

The scan ranges (δ_x, δ_z) and tilt angle (ϕ) of both piezoelectric tube actuators in Figure 3.1 are modelled using the finite-element (FE) package ANSYS. Due to symmetry, δ_y is identical to δ_x and is omitted for brevity. Both tubes are made of PZT-5H piezoelectric ceramic material having length 50.8 mm, thickness 0.66 mm and outer diameter 9.5 mm. FE simulations of the tubes are shown in Figure 3.3. For the conventional tube, the length of the of the Z electrode is half that of the X and Y electrodes. An aluminium sample platform, which serves as a sensor target in experiments, is also modelled. The piezoelectricity of the tube is modelled using the ANSYS PiezoAndMEMS Application

Table 3.1: Voltages applied to simulate lateral and vertical deflections of piezoelectric tube actuators.

Tube	Def.	$V_{X+/-}$	$V_{Y+/-}$	V_i	V_z
Conventional	δ_x	± 200	0	0	0
Conventional	δ_z	0	0	0	± 200
Proposed	δ_x	± 200	0	0	N/A
Proposed	δ_z	0	0	-200	N/A

Customization Toolkit extension. Table 2.1 lists the piezoelectric coefficients in stress form (e), the relatively permittivity ϵ^S/ϵ_o and the piezoelectric constant d_{31}. A cylindrical coordinate system is used to define the polarization vector of the actuator in the model, that is radially inwards. The input voltages shown in Table 3.1 are applied to the conventional and proposed tubes for simulating the maximum scan range and cross-coupling. FE results in Table 3.2 indicate an 18% increase in lateral scan range and 52% increase in vertical scan range of the proposed technique compared to the conventional one. The normalised cross-coupling (ϕ/δ_x) is also increased by about 29% primarily due to the increase in the tilt angle and a larger strain experienced by the proposed tube.

Table 3.2: Comparisons of maximum deflections and cross-coupling of the conventional and proposed piezoelectric tube actuators.

Axis driven	Def.	FE simulated		Experiment	
		Conv.	Proposed	Conv.	Proposed
X	δ_x (μm)	± 14.69	± 17.4	± 26.24	± 42.4
	ϕ (μrad)	± 372.67	± 572.67	± 740.6	$\pm 1486.7.3$
	ϕ/δ_x (rad/m)	25.4	32.9	28.2	35.1
	δ_z (μm)	0.00015	-0.0044	-0.0188	-0.0635
Z	δ_z (μm)	± 0.92	-2.8	± 1.81	-6.77

3.4 Experiments

Figure 3.4 shows the experiment setup. Two MicroSense 6810 capacitive sensors are used to measure the vertical displacement and tilt angle. A MicroSense 4810 capacitive sensor is used to measure the lateral displacement (X axis). All three sensors have a sensitivity of 10 μm/V. PiezoDrive TD250 high-voltage amplifier with a gain of 25 V/V, is used to drive the tube actuators. The X+ electrode is connected to the non-inverted amplifier while the X- electrode is connected to the inverted amplifier. A dSPACE MicroLabBox prototyping system is used to generate input references and to record the sensor measurements. To generate X-displacement, a 1-Hz sinusoidal reference of 8 V amplitude is applied to the amplifiers, which is amplified to $\pm$200 V. For the conventional tube, the length of the X- and Z-electrode is 31.5 mm and 15.7 mm respectively. The vertical motion of the conventional tube is generated by applying the same sinusoidal signal to the Z-electrode while the internal electrode is grounded. For the proposed tube, the internal electrode is driven by a 1-Hz sinusoidal reference with a magnitude of 0 V to -200 V.

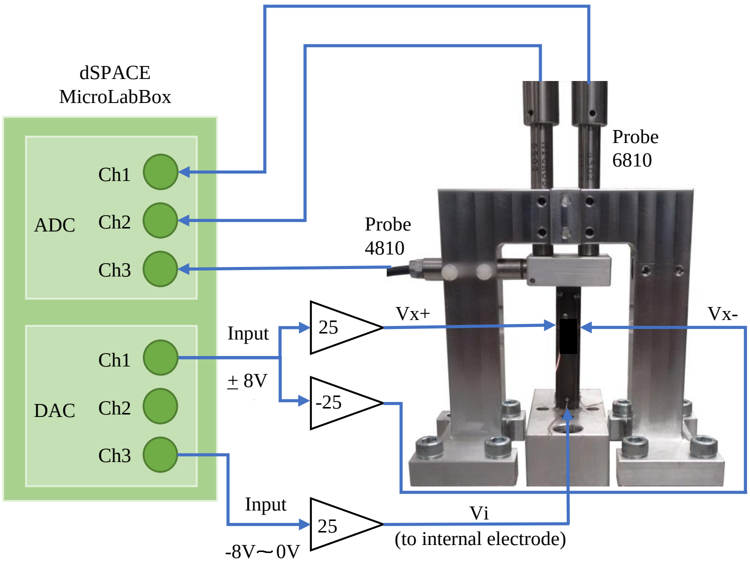

Figure 3.4: Experimental setup for deflection measurements of the piezoelectric tube actuator.

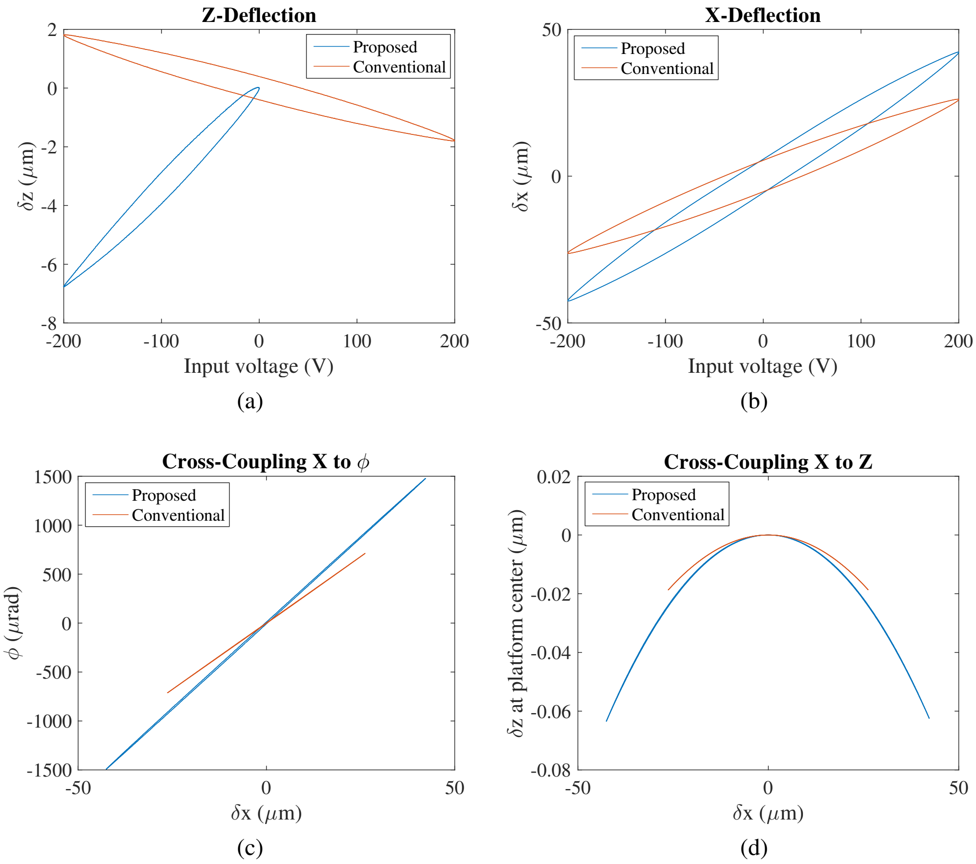

Figure 3.5: Measured deflections δ_x and δ_z and cross-coupling X to ϕ and X to Z of conventional and proposed tube actuators.

3.5 Results and Comparisons

The measured displacements and cross-coupling of the conventional and proposed tube actuators are compared in Table 3.2 and plotted in Figure 3.5. Experimental results indicate a 62% increase in the lateral scan range and a 86% increase in the vertical scan range. The normalised cross-coupling ϕ/δ_x also increases by 24% as this is proportional to the electrode length. The hysteresis exhibited in the X-axis is 13.6% of the scan range for the proposed method, and 20.4% for the conventional method. For vertical motion, the hysteresis is 15.8% for the proposed method, and 21.9% for the conventional method.

The discrepancies between the simulated and experimental results are partially due to uncertainty in d_{31}. Piezoelectric constants are estimated for small-signals. Due to non-linearity of the piezoelectric material (as observed in Figure 3.5), significant differences in d_{31} values are found when the full voltage range is applied [47]. To demonstrate this, d_{31} is measured at -10 V and -200 V and is found to increase by 44% from 305 pm/V to 440 pm/V.

Chapter 4

A New Actuation Technique for an Eight-electrode Piezoelectric Tube Actuator

4.1 Introduction

This chapter describes a new electrical configuration for piezoelectric tube actuators which eliminates the tilting and vertical cross-coupling at the moving end, and significantly increases the vertical scan range. As discussed in the previous chapters, the outer surface of a conventional piezoelectric tube [40, 41] has quartered X-, Y-electrodes covering two-third of its length for lateral actuation and a circumferential Z-electrode covering one-third of its length for vertical actuation as shown in Figure 4.1(a). The inner surface is grounded. During bending, the angular motion of the tube causes the moving platform to tilt from its original horizontal plane. The tilt angle distorts interference pattern in optical microscopy [44] and reduces image quality in atomic force microscopy [42]. To reduce the tilt angle, an eight-electrode tube actuator was proposed where the outer electrodes are split to create upper and lower sections. When applying voltages with the same magnitude on the X- or Y-electrode but with opposite polarity at the two halves, the tube bends in a sigmoid shape which reduces the tilt angle significantly. In [42], voltage is applied to the outer circumferential Z-electrode of the eight-electrode tube to generate vertical displacement.

This chapter proposes to eliminate the outer circumferential Z-electrode and drive the inner electrode with a negative voltage instead of grounding it, as shown in Figure 4.1(b). The entire length of the tube is therefore used to generate significantly larger vertical displacements. Eliminating the Z-electrode also allows longer and perfectly symmetrical quadrant electrodes, which increases the lateral scan range and eliminates both tilting and vertical cross-coupling. The first contribution of this chapter is a description of the eight-electrode configuration with a driven internal electrode. The second contribution is a detailed mechanical analysis of the eight-electrode configuration, including the deflection sensitivity and proof of tilt elimination.

4.2 Analytical Estimations of Deflections

4.2.1 Considering a thin tube using Newton's laws

The lateral and vertical deflections of the proposed eight-electrode tube are modelled using the Euler-Bernoulli beam theory. The modelling establishes that a voltage applied to the inner electrode results

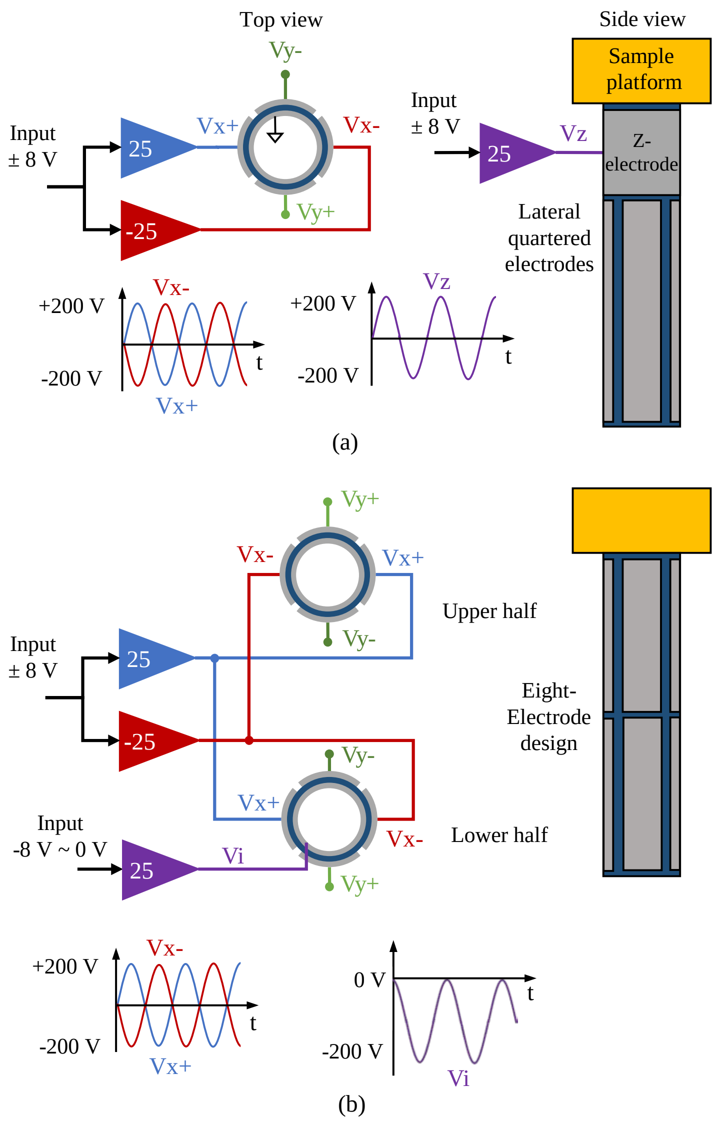

Figure 4.1: Electrode configuration and driving method for the (a) conventional piezoelectric tube, and (b) eight-electrode tube.

in vertical motion which is independent of the differential voltages applied to the external electrodes. For deflection along the Y-axis, the upper and lower pairs of the quartered Y-electrodes are actuated with $\pm V_y$ volts and the internal electrode with V_i volts as described in Figure 4.2. The X-electrodes are grounded. Cylindrical coordinates (z, r, θ) are employed in the modelling due to the shape of the tube. The transformation $(x, y) = (-rcos\theta, -rsin\theta)$ converts cartesian coordinates to cylindrical co-

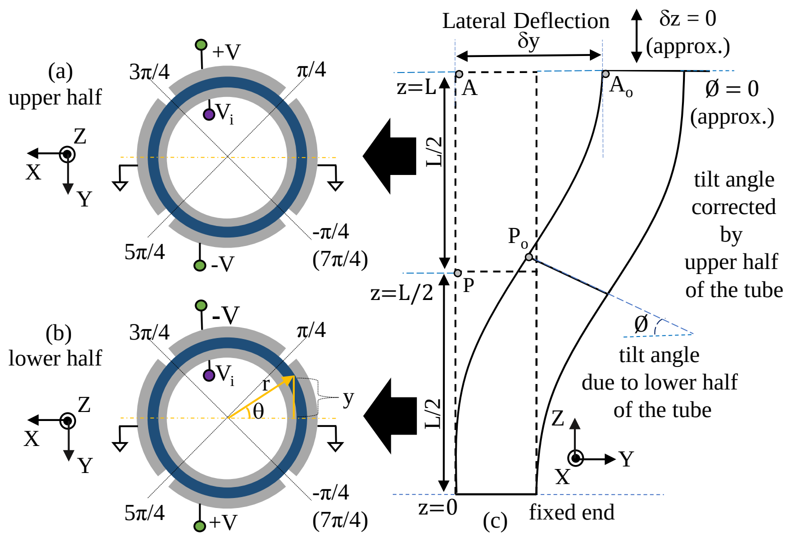

Figure 4.2: The Y-electrodes are driven with $\pm V_y$ in the upper and lower half of the tube. The internal electrode is driven with V_i. The X-electrodes are connected to ground.

ordinates. The voltage $V(z,\theta)$ applied is

$$V(z,\theta)=\begin{cases} -V_y - V_i, & \theta \in \left(\frac{\pi}{4},\frac{3\pi}{4}\right), \quad z<\frac{L}{2} \\ V_y - V_i, & \theta \in \left(\frac{5\pi}{4},\frac{7\pi}{4}\right), \quad z<\frac{L}{2} \\ V_y - V_i, & \theta \in \left(\frac{\pi}{4},\frac{3\pi}{4}\right), \quad z>\frac{L}{2} \\ -V_y - V_i, & \theta \in \left(\frac{5\pi}{4},\frac{7\pi}{4}\right), \quad z>\frac{L}{2} \\ 0, & \text{otherwise.} \end{cases} \tag{4.1}$$

For a thin tube, a parallel plate capacitive structure is used to approximate the electric field distribution in the tube. The radial electric field is given by

$$E_3(z,r,\theta) = V(z,\theta)/h, \tag{4.2}$$

where h is the thickness of the tube. Applying Euler-Bernoulli kinematic assumptions [46], the strain is

$$S_1(z,r,\theta) = -r\sin(\theta)w_0''(z), \tag{4.3}$$

where $w_0(z)$ is the lateral deflection. Due to the split in the outer electrode at $z=\frac{L}{2}$, $w_0''(z)$ is evaluated for the upper and lower sections separately,

$$w_0''(z)=\begin{cases} w_1''(z) & z\in(0,\frac{L}{2}) \\ w_2''(z) & z\in(\frac{L}{2},L) \end{cases}. \tag{4.4}$$

The constitutive equations of the piezoelectric material are

$$T_1 = ES_1 - e_{31}E_3, \tag{4.5}$$

$$D_3 = e_{31}S_1 + \varepsilon_{33}E_3, \tag{4.6}$$

where T_1 is the stress, E is the elastic modulus, e_{31} is the piezoelectric coefficient, D_3 is the electric displacement, and ε_{33} is the permittivity. Substituting E_3 and S_1 into (4.5) results in the following expression for the stress in the tube,

$$T_1(z, r, \theta) = Er\sin(\theta)w_0''(z) - e_{31}V(z, \theta)/h. \tag{4.7}$$

The first term of this expression is the stress exerted by the material and the second term is the stress due to the piezoelectric effect. These stresses induce moments about the neutral axis of the tube. The total moment on the cross-sectional area is

$$M(z) = \int_\theta yT_1 \,\mathrm{d}\theta. \tag{4.8}$$

$M(z)$ is evaluated for upper and lower sections separately,

$$M(z) = \begin{cases} M_1(z) & z \in (0, \frac{L}{2}) \\ M_2(z) & z \in (\frac{L}{2}, L) \end{cases}. \tag{4.9}$$

For a thin tube of radius r_0, $y = -r_0\sin(\theta)$, therefore $M_1(z)$ is evaluated as

$$\begin{aligned} M_1(z) &= \int_\theta -r_0\sin(\theta)T_1 \,\mathrm{d}\theta \\ &= -\int_{-\pi/4}^{\pi/4} Er_0^2\sin^2(\theta)w_1''(z)d\theta \\ &\quad -\int_{\pi/4}^{3\pi/4} [Er_0^2\sin^2(\theta)w_1''(z) - e_{31}r_0 sin(\theta)\frac{(-V_y - V_i)}{h}]d\theta \\ &\quad -\int_{3pi/4}^{5\pi/4} Er_0^2\sin^2(\theta)w_1''(z)d\theta \\ &\quad -\int_{5pi/4}^{7\pi/4} [Er_0^2\sin^2(\theta)w_1''(z) - e_{31}r_0 sin(\theta)\frac{(V_y - V_i)}{h}]d\theta \\ &= -Er_0^2w_1''(z)\pi + \frac{\sqrt{2}e_{31}r_0}{h}(-V_y - V_i - V_y + V_i) \\ &= -Er_0^2w_1''(z)\pi - \frac{2\sqrt{2}e_{31}r_0V_y}{h} \end{aligned} \tag{4.10}$$

Similar evaluation for $M_2(z)$ gives

$$M_2(z) = -Er_0^2w_2''(z)\pi + \frac{2\sqrt{2}e_{31}r_0V_y}{h}. \tag{4.11}$$

Note that the voltage V_i of the inner electrode is eliminated in the moment expression which shows that V_i has no effect on the lateral displacement of the tube. With no external load, the net moment on the cross-sectional area is zero when in equilibrium and is evaluated in the upper and lower sections as

$$M_1(z) = -Er^2w_1''(z)\pi - \frac{2\sqrt{2}e_{31}r_0V_y}{h} = 0, \tag{4.12}$$

$$M_2(z) = -Er^2w_2''(z)\pi + \frac{2\sqrt{2}e_{31}r_0V_y}{h} = 0. \tag{4.13}$$

Rearranging and substituting $r_0 = D/2$ and $e_{31} = Ed_{31}$, where D is the diameter, and d_{31} is the piezoelectric strain constant, the above equations give

$$w_1''(z) = -\frac{4\sqrt{2}d_{31}V_y}{hD\pi}, \quad w_2''(z) = \frac{4\sqrt{2}d_{31}V_y}{hD\pi}. \tag{4.14}$$

Integrating w_1'',

$$w_1'(z) = \phi_1(z) = -Kz + C_1, \tag{4.15}$$

$$w_1(z) = -\frac{z^2K}{2} + C_1z + C_2. \tag{4.16}$$

where $K = 4\sqrt{2}d_{31}V_y/(hD\pi)$. Applying boundary conditions $w_1'(0) = 0$ and $w_1(0) = 0$ results in $C_1 = 0$ and $C_2 = 0$. Similarly integrating w_2'', and applying boundary conditions $w_1'(\frac{L}{2}) = w_2'(\frac{L}{2})$ and $w_1(\frac{L}{2}) = w_2(\frac{L}{2})$ results in $C_3 = -KL$ and $C_4 = \frac{KL^2}{4}$. Substituting these constants into w_2, the deflection of the eight-electrode tube actuator at $z = L$ is

$$\delta_y = w_2(L) = -\frac{\sqrt{2}d_{31}L^2V_y}{\pi Dh}. \tag{4.17}$$

That is, the deflection of the eight-electrode configuration is half that of the four-quadrant configuration [45]. This is the trade-off required to eliminate tilting and cross-coupling. Similarly, the deflection equation in the X-axis is

$$\delta_x = -\frac{\sqrt{2}d_{31}L^2V_x}{\pi Dh}. \tag{4.18}$$

For vertical motion, the standard axial extension equation is

$$\delta_z = -\frac{d_{31}LV_i}{h}, \tag{4.19}$$

where V_x, V_y, and V_i are the magnitudes of electrode voltages for the X, Y and Z axis respectively. In the experimental setup, the voltages V_x and V_y and are kept in the range [-200, 200] and V_i is in the range [-200, 0].

4.2.2 Considering a thick tube using Hamilton's principle

The physical principle used to derive the equations of motion in this section is Hamilton's principle. Evaluation of Hamilton's principle requires the electromechanical enthalpy and kinetic energy of the structure as a function of the desired input and output variables. The inputs of the system are voltages applied to the tube's electrodes. The output is the lateral and vertical deflections of the tube. These input and output variables are related to the electric and strain fields in the structure respectively. With expressions for the stress and electric field, along with the constitutive equations of the material, the enthalpy and kinetic energy are evaluated.

The stress field

The piezoelectric tube actuator is modeled as a one-dimensional structure. Beam dynamics model the lateral deflection, and bar dynamics model the axial (vertical) displacement. Euler-Bernoulli kinematics

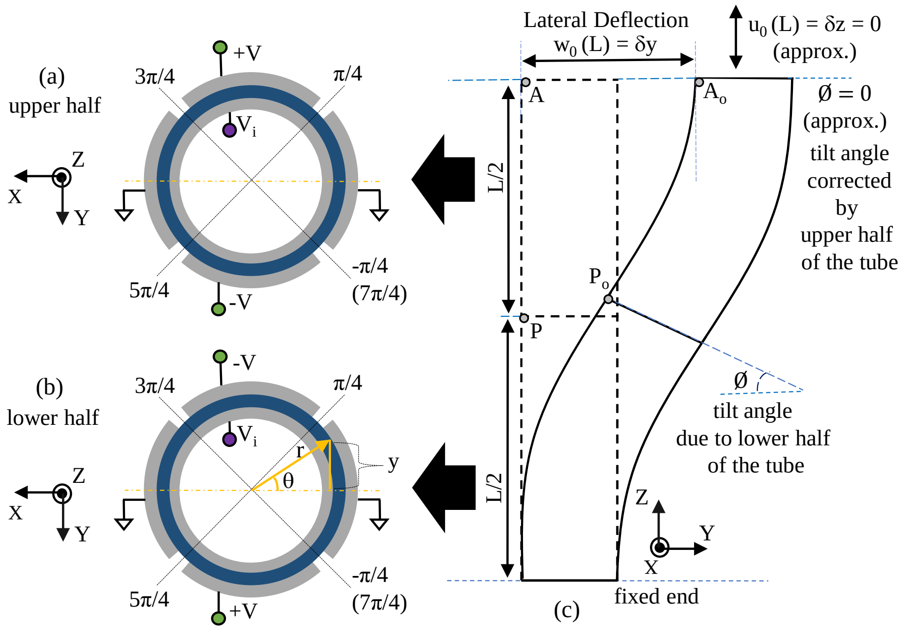

Figure 4.3: The Y-electrodes are driven with equal but opposite voltages V_y in the upper and lower half of the tube. The internal electrode is driven by V_i. The X-electrodes are grounded.

are assumed for the beam deflections. Due to the cylindrical shape of the tube, the cylindrical coordinates (z, r, θ) are used in this analysis. The displacement field of the tube is [48, 49]

$$u_1(z, r, \theta) = u_0(z) + rsin(\theta)w_0'(z), \tag{4.20}$$
$$u_2(z, r, \theta) = 0, \tag{4.21}$$
$$u_3(z, r, \theta) = w_0(z), \tag{4.22}$$

where (u_1, u_2, u_3) are the displacements along the z, x, and y axes respectively and the prime $(')$ indicates the derivative with respect to z. This displacement field is parameterized in terms of the one-dimensional quantities, that is the y-axis deflection w_0 and the axial displacement u_0. From the strain-displacement relationship [50, 51], there is only one non-zero strain component associated with these kinematics,

$$S_1(z, r, \theta) = u_1'(z, r, \theta) = u_0'(z) + r\sin(\theta)w_0''(z). \tag{4.23}$$

The electric field

The electric field needs to be parameterized in terms of the applied voltages. A cylindrical capacitive structure is assumed. The polarization of the tube is radial. The electric field is given by

$$E_3(z, r, \theta) = \frac{V(z, \theta)}{r\ln(r_2/r_1)}, \tag{4.24}$$

where r_2 is the outer radius of the tube, r_1 is the inner radius of the tube, and the electrode voltage $V(z,\theta)$ takes the value at each quadrant of the tube,

$$V(z,\theta) = \begin{cases} 0, & \theta \in \left(-\frac{\pi}{4}, \frac{\pi}{4}\right) \\ -V_H - V_i, & \theta \in \left(\frac{\pi}{4}, \frac{3\pi}{4}\right) \\ 0, & \theta \in \left(\frac{3\pi}{4}, \frac{5\pi}{4}\right) \\ V_H - V_i, & \theta \in \left(\frac{5\pi}{4}, \frac{7\pi}{4}\right) \end{cases} . \tag{4.25}$$

where

$$V_H(z) = V_y\left(1 - 2H(z - \tfrac{L}{2})\right). \tag{4.26}$$

The voltage V_y is applied to the outer electrodes with positive and negative polarities as shown in Figure 4.3. V_i is the voltage applied to the inner electrode. $H()$ is the Heaviside step function defined as

$$H(z) = \begin{cases} 1, & z > 0 \\ 0, & z < 0 \end{cases} , \tag{4.27}$$

which is used to model the split in the electrodes in the middle of the tube.

The constitutive equations

Since there is only a single non-zero component of both the strain field and the electric field, the constitutive equations of the piezoelectric material simplify to [8]

$$T_1 = ES_1 - e_{31}E_3, \tag{4.28}$$

$$D_3 = e_{31}S_1 + \varepsilon_{33}E_3, \tag{4.29}$$

where E is Young's modulus, e_{31} is the piezoelectric coefficient, ε_{33} is the dielectric permittivity, T_1 is the stress, and D_3 is the electric displacement.

The enthalpy and kinetic energy

Considering the non-zero components of the stress, strain, electric field, and electric displacement, the electromechanical enthalpy of the piezoelectric material is [52]

$$H = \frac{1}{2}\int_{\Omega} T_1S_1 - D_3E_3\, d\Omega, \tag{4.30}$$

where Ω is the domain defined by the volume of the structure. Substituting (4.23), (4.24), (4.28) and (4.29) into (4.30), the enthalpy in terms of the extension u_0, deflection w_0, and voltages (V, V_i) is

$$\begin{aligned} H = \int_0^L & \frac{EA}{2}\left(u_0'\right)^2 + \frac{EI}{2}\left(w_0''\right)^2 + k_E V_i u_0' \\ & + k_B V_H w_0'' + 2k_C V^2 + 2k_C V_i^2\, dz, \end{aligned} \tag{4.31}$$

which gives,

$$A = \pi \left(r_2^2 - r_1^2\right), \tag{4.32}$$

$$I = \frac{\pi}{4} \left(r_2^4 - r_1^4\right), \tag{4.33}$$

$$k_E = \frac{\pi e_{31}(r_2 - r_1)}{2 \ln(r_2/r_1)}, \tag{4.34}$$

$$k_B = \frac{\sqrt{2} e_{31}(r_2^2 - r_1^2)}{\ln(r_2/r_1)}, \tag{4.35}$$

$$k_C = \frac{-\varepsilon_{33}\pi}{4 \ln(r_2/r_1)}. \tag{4.36}$$

where the A is the area, I is the moment of inertia, constants k_E and k_B characterize the electromechanical coupling and relate the input voltage to the deflection, and the constant k_C relates the input voltage to the stored capacitive energy.

The kinetic energy is a function of the velocity field which is found by taking the derivative with respect to time of the displacement field. The kinetic energy T is [8, 52]

$$T = \frac{1}{2} \int_\Omega \rho \left(\dot{u_1}^2 + \dot{u_2}^2 + \dot{u_3}^2\right) \, d\Omega, \tag{4.37}$$

$$= \frac{1}{2} \int_0^L \rho A \left(\dot{u}_0\right)^2 + \rho A \left(\ddot{w}_0\right)^2 + \rho I \left(\dot{w}_0'\right)^2 \, dz, \tag{4.38}$$

where the dot $(\dot{})$ indicates the derivate with respect to time. The Euler-Bernoulli beam theory assumes that the rotary inertia is insignificant compared to the translational inertia [53], therefore the kinetic energy becomes

$$T = \frac{1}{2} \int_0^L \rho A \left(\dot{u}_0\right)^2 + \rho A \left(\ddot{w}_0\right)^2 \, dz. \tag{4.39}$$

The characteristic equations

Hamilton's principle introduces a fundamental variational principle from which the mechanics of the tube positioner can be derived. For this class of problem Hamilton's principle is expressed as [48, 51, 52, 54, 55]

$$\delta \int_{t_1}^{t_2} T - H \, dt = 0, \tag{4.40}$$

where δ is the variational operator. The evaluation of Hamilton's principle in (4.40) requires the application of variational calculus. Hamilton's principle is evaluated for the differential equations and natural boundary conditions that govern the the extension and deflection of the tube. Essential boundary conditions exist at the fixed end $(z = 0)$ enforcing zero deflection $(w_0(0) = 0)$, zero extension $(u_0(0) = 0)$, and zero rotation $(w_0'(0) = 0)$. The analysis results in the system for extension being separable from the system for deflection.

The extension characteristic equations and boundary conditions are

$$\rho A \ddot{u}_0 - EA u_0'' - k_E V_i = 0, \tag{4.41}$$

$$EA u_0' + k_E V_i = 0 \qquad \text{at } x = L, \tag{4.42}$$

$$u_0 = 0 \qquad \text{at } x = 0. \tag{4.43}$$

Table 4.1: Parameters of the tube.

Parmeter	Value
d_{31} ($\times 10^{-12}$m/V)	-274
r_1 (mm)	4.09
r_2 (mm)	4.75
L (mm)	50.8

And the deflection characteristic equations and boundary conditions are

$$\rho A \ddot{w}_0 + EI w_0'''' + k_B V_H'' = 0, \tag{4.44}$$

$$k_B V_H + EI w_0'' = 0 \qquad \text{at } x = L, \tag{4.45}$$

$$k_B V_H' + EI w_0''' = 0 \qquad \text{at } x = L, \tag{4.46}$$

$$w_0 = 0 \qquad \text{at } x = 0, \tag{4.47}$$

$$w_0' = 0 \qquad \text{at } x = 0. \tag{4.48}$$

Static deflection and rotation of the tube

Set the dynamic term to zero and start integrating the differential equation in (4.44)

$$EI w_0'''' + k_B V_H'' = 0, \tag{4.49}$$

$$EI w_0''' + k_B V_H' + c_1 = 0, \tag{4.50}$$

$$EI w_0'' + k_B V_H + c_1 x + c_2 = 0. \tag{4.51}$$

The constants of integration $c_1 = 0$ and $c_2 = 0$ due to the boundary conditions in (4.45) and (4.46). Next substitute in the expression for V_H

$$EI w_0'' + k_B V_y - 2 k_B V_y H\left(z - \tfrac{L}{2}\right) = 0 \tag{4.52}$$

$$EI w_0' + k_B V_y z - 2 k_B V_y \left(z - \tfrac{L}{2}\right) H\left(z - \tfrac{L}{2}\right) + c_3 = 0 \tag{4.53}$$

$$\begin{aligned} EI w_0 + \tfrac{1}{2} k_B V_y z^2 - k_B V_y \left(z - \tfrac{L}{2}\right)^2 H\left(z - \tfrac{L}{2}\right) \\ + c_3 x + c_4 = 0 \end{aligned} \tag{4.54}$$

Due to the essential boundary conditions in (4.47) and (4.48), the constants of integration $c_3 = 0$ and $c_4 = 0$. Therefore the deflection and rotation of the beam is

$$w_0'(z) = \frac{k_B V_y}{EI}\left(-z + 2\left(z - \tfrac{L}{2}\right) H\left(z - \tfrac{L}{2}\right)\right), \tag{4.55}$$

$$w_0(z) = \frac{k_B V_y}{EI}\left(-\tfrac{1}{2} z^2 + \left(z - \tfrac{L}{2}\right)^2 H\left(z - \tfrac{L}{2}\right)\right). \tag{4.56}$$

The deflection and rotation at the end of the tube $(z = L)$ are

$$w_0'(L) = \phi = 0, \tag{4.57}$$

$$w_0(L) = \delta_y = -\frac{k_B L^2}{4EI} V_y. \tag{4.58}$$

Evaluating the deflection at the free-end of the tube with parameters in (4.1), and $e_{31} = E d_{31}$, the deflection sensitivity of the tube is 54.153 nm/V. At V = 200 V, the deflection δ_y of the tube is 10.831 μm.

4.3 Finite-Element-Analysis

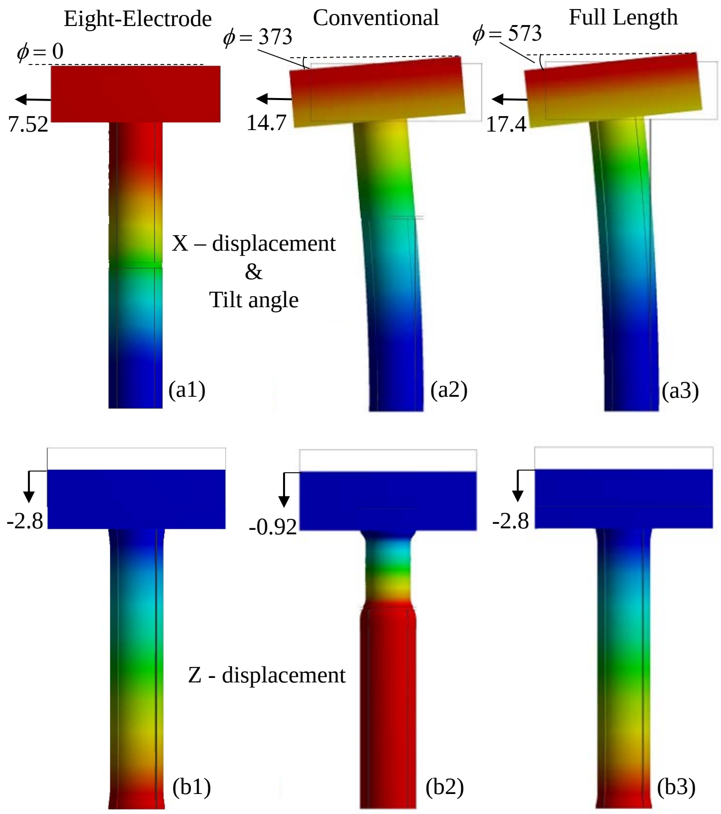

Figure 4.4: (a) FE simulated deflection (in μm) and tilt angle (in μrad) of an eight-electrode (a1 & b1), the conventional (a2 & b2) and the full length (a3 & b3) piezoelectric tube actuators.

The maximum scan ranges (δ_x, δ_z), and cross-coupling from δ_x to ϕ and from δ_x to δ_z are simulated and compared for the cases of the conventional tube, the eight-electrode tube and the proposed full-length tube. All the three tubes are made of PZT-5H piezoelectric ceramic material having length 50.8 mm, thickness 0.66 mm and outer diameter 9.5 mm. ANSYS workbench is used to conduct the finite-element (FE) modeling in static mode as shown in Figure 4.4. For the conventional tube, the length of the outer circumferential Z-electrode is half of that of the quartered X and Y electrodes. An aluminium holder which serves as a sensor target in experiments is also modeled. The piezoelectric property of the tube is modeled using the ANSYS PiezoAndMEMS Application Customization Toolkit extension. Table 2.1 lists the piezoelectric coefficients in stress form (e), the relatively permittivity ϵ^S/ϵ_o and the piezoelectric constant d_{31}. A cylindrical coordinate system is used to define the polarization vector of the actuator in the model and is radially inwards. Input voltages are applied to the conventional and the eight-electrode tube as illustrated in Figure 4.1(a) and (b). For the full-length tube, the actuation configuration can be found in Figure 3.1. Table 4.2 shows the driving configuration for all the three tube models.

FE results for the eight-electrode tube in Table 4.3 indicate a decrease in the lateral scan range by 49% and 57% compared to that of the conventional and full-length tube respectively. This is expected due to the decrease in the electrode length. However, the eight-electrode tube shows negligible vertical cross-coupling motion and tilt angle compared to the other two tubes. The vertical scan range of the eight-electrode tube is also increased by 52% compared to the conventional tube due to the used of the

Table 4.2: Voltages applied to simulate the lateral and vertical deflections.

Tube	Def.	$V_{X+/-}$	$V_{Y+/-}$	V_i	V_z
Eight-electrode	δx	± 200	0	0	N/A
Eight-electrode	δz	0	0	-200	N/A
Conventional	δx	± 200	0	0	0
Conventional	δz	0	0	0	± 200
Full-length	δx	± 200	0	0	N/A
Full-length	δz	0	0	-200	N/A

Table 4.3: Comparisons of maximum deflections and cross-coupling of the eight-electrode, conventional and full-length piezoelectric tube actuators.

Axis Driven	Deflection	FE Simulated Results		
		Eight-electrode	Conventional	Full-length
X	δ_x (μm)	± 7.52	± 14.69	± 17.4
	ϕ (μrad)	± 0.67	± 372.67	± 572.67
	ϕ/δ_x (rad/m)	0.09	25.4	32.9
	δ_z (μm)	-0.000058	0.00015	-0.0044
Z	δ_z (μm)	-2.8	± 0.92	-2.8
Axis Driven	**Deflection**	**Experimental Results**		
		Eight-electrode	**Conventional**	**Full-length**
X	δ_x (μm)	± 14.73	± 26.24	± 42.4
	ϕ (μrad)	± 17.1	± 740.6	± 1486.7
	ϕ/δ_x (rad/m)	1.16	28.22	35.06
	δ_z (μm)	-0.006	-0.0188	-0.0635
	δ_z/δ_x ($\times 10^{-4}$)	4.07	7.16	14.97
Z	δ_z (μm)	-5.22	± 1.81	-6.77

larger inner electrode.

4.4 Experiments

Figure 4.5 shows the experiment setup for the eight-electrode tube actuator. Two MicroSense 6810 capacitive sensors are used to measure the vertical displacement δ_z and the tilt angle ϕ. A MicroSense 4810 capacitive sensor is used to measure the lateral deflection δ_x. All three sensors have a sensitivity of 10 μm/V. PiezoDrive TD250 high-voltage amplifier with a gain of 25 V/V is used to drive the piezoelectric tube actuators. A dSPACE MicroLabBox prototyping system is used to generate input references and record the sensor measurements. Driving configurations of the three piezoelectric tube actuators can be found in Table 4.2. To generate X-displacement, a 1-Hz sinusoidal reference of ± 8 V is amplified to ± 200 V and drives the tubes. For both the eight-electrode and full-length tube actuators, negative voltages in the range of -200 V to 0 V are applied to their inner electrodes to produce vertical displacements. For the conventional tube, the circumferential Z-electrode is driven with ± 200 V while keeping the internal electrode at ground to produce Z-displacement.

Note that all experiments were conducted at low frequencies. High-frequency applications are be-

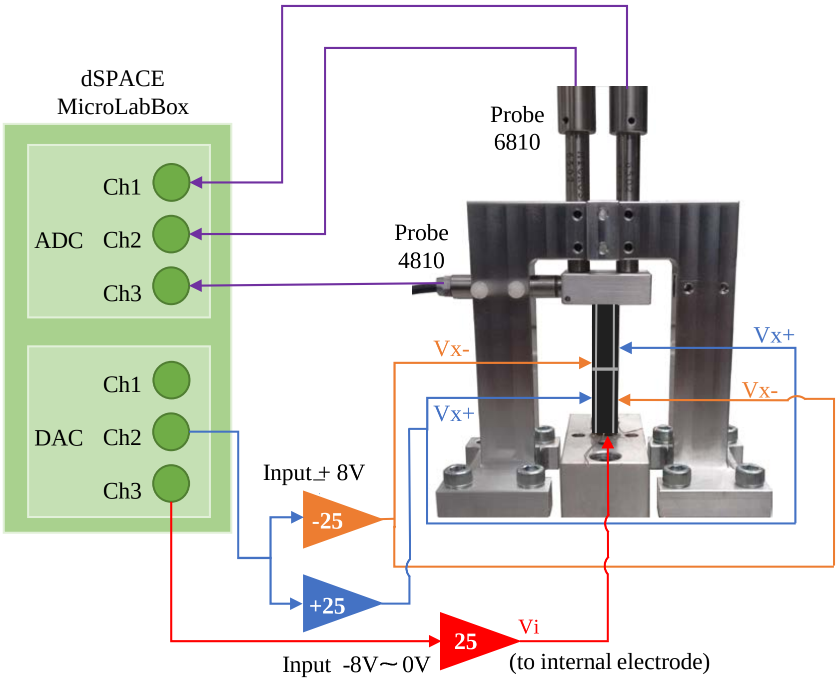

Figure 4.5: Experimental setup for deflection measurements of the eight-electrode piezoelectric tube actuator.

yond the scope of this thesis.

4.5 Results and Comparisons

The measured displacements and tilt angles of the three tubes are summarized in Table 4.3. Experimental results are plotted in Figure 4.6. The lateral scan range δ_x of the eight-electrode actuator is 44% and 65% less than that of the conventional tube and the full-length tube actuators respectively. This is expected because of the shorter electrode length used in the eight-electrode tube. However, the normalised tilting ϕ/δ_x is reduced by 96% and 97% respectively. The normalised vertical cross-coupling δ_z/δ_x is also reduced by 43% and 73% respectively. The proposed actuation method increases the δ_z range by 44% compared to that of the conventional tube actuator. Although the eight-electrode tube has the same length as that of the full-length tube, there is a discrepancy in the measured δ_z due to different inner electrode length caused by manufacturing imperfections.

The hysteresis exhibited in the X-axis is 17.5%, 20.4% and 13.5% of the full scan range for the eight-electrode, conventional and full-length actuators respectively. The hysteresis exhibited in the Z-axis is 14.7%, 22% and 15.8% respectively.

The discrepancies between the simulated and experimental results are partially due to uncertainty in d_{31}. Piezoelectric constants are estimated for small-signals. Due to non-linearity of the piezoelectric material (as observed in Figure 4.6), significant differences in d_{31} values are found when the full voltage range is applied [47]. During experiments on the full-length tube, the d_{31} is found to increase from 305 pm/V to 440 pm/V when the tube is driven at -10 V and -200 V respectively.

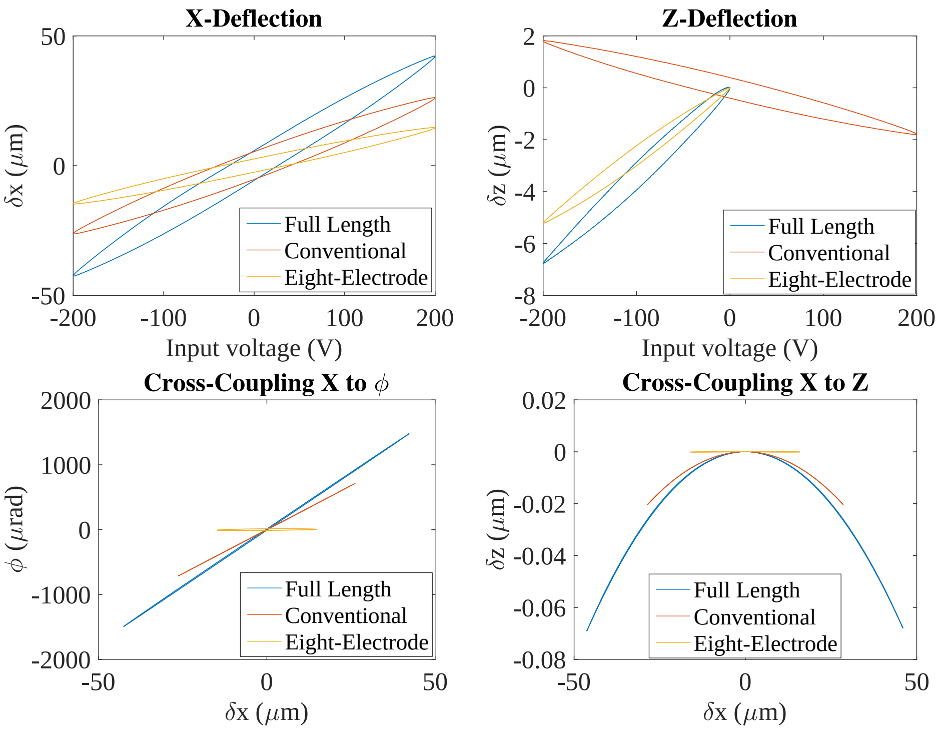

Figure 4.6: Measured deflections δ_x and δ_z and cross-coupling from X to ϕ and from X to Z of the eight-electrode, conventional and proposed tube actuators.

Chapter 5

Conclusions and Future Work

The thesis describes new methods for increasing the scan range and reducing unwanted motion in piezoelectric tube actuators. Contributions of this thesis are summarised as follows.

Chapter 1 introduces the piezoelectric effect and the constitutive equations of piezoelectric actuators. The piezoelectric tube actuator and its applications are described. The limitations are also discussed in detail, which include: low scan range, vertical cross-coupling, and tilting.

Chapter 2 analyzes the effect of varying the electrode length on the lateral deflection and tilting. The percentage of reduction in lateral deflection (δ_x) and tilt angle (ϕ) are simulated in ANSYS workbench. The analysis identifies a trade-off between the tilt angle and scan range. Tilting can be reduced by 40% without compromising the lateral deflection by more than 22.6%.

Chapter 3 proposed a new electrical configuration for increasing the lateral and vertical scan range of piezoelectric tube actuators. By driving the internal electrode rather than connecting it to ground, the need for a circumferential electrode is eliminated. This results in longer quadrant electrodes which produce larger lateral deflections. FE models were constructed in ANSYS workbench to simulate the lateral and vertical scan range, as well as the tilting and the vertical cross-coupling. Experimental results show a 62% increase in lateral scan range and an 86% increase in the vertical scan range.

Chapter 4 proposed a new electrical configuration for piezoelectric tube actuators which eliminated the tilting and vertical cross-coupling at the moving end, and significantly increases the vertical scan range. The piezoelectric tube actuator has an upper and a lower quartered-electrode. When applying voltages with the same magnitude on the X- or Y-electrode but with opposite polarity at the two halves, the tube bends in a sigmoid shape which eliminates the tilting. To increase the vertical deflection, negative voltages were applied to the internal electrode. FE models were constructed in ANSYS workbench to simulate the lateral and vertical scan range, as well as the tilting and the vertical cross-coupling. Experimental results showed that the vertical scan range of the eight-electrode tube was increased by 44% compared to that of the conventional tube. The tilting and vertical cross-coupling was reduced by 96% and 43% respectively. However, the lateral scan range was 44% less than the conventional tube due to the shorter electrode length used.

Future extension of this work could focus on a number of areas to optimize the performance of piezoelectric tube actuators. The first topic worthy of attention is the mechanical geometry of the tube, which is presently chosen using an ad-hoc method. An alternative would be to optimize the diameter and length to minimize the resonance frequency whilst achieving a desired scan-range.

Although this thesis is primarily concerned with passive methods for performance improvement, there is also sufficient scope for active compensation methods. A significant literature has developed on the control of piezoelectric tube scanners; however, these methods require the addition of sensors which may be significantly larger or more costly than the tube itself. By incorporating resistive strain sensors, or piezoresistive strain sensors, onto the tube surface, compact and low-cost closed-loop control could be realized.

Bibliography

[1] A J Fleming and K K Leang. *Design, modeling and control of nanopositioning systems*. Springer, 2014.

[2] H Jaffe and D A Berlincourt. Piezoelectric transducer materials. *Proceedings of the IEEE*, 53(10):1372–1386, 1965.

[3] Ltd APC International. *Piezoelectric ceramics: principles and applications*. APC International, 2002.

[4] J A Gallego-Juarez. Piezoelectric ceramics and ultrasonic transducers. *Journal of Physics E: Scientific Instruments*, 22(10):804, 1989.

[5] J F Tressler, S Alkoy, and R E Newnham. Piezoelectric sensors and sensor materials. *Journal of electroceramics*, 2(4):257–272, 1998.

[6] AWWAH Meitzler, HF Tiersten, AW Warner, D Berlincourt, GA Couqin, and FS Welsh III. Ieee standard on piezoelectricity, 1988.

[7] A Erturk and D J Inman. Appendix a: piezoelectric constitutive equations. *Piezoelectric Energy Harvesting*, pages 343–348, 2011.

[8] A Preumont. *Vibration Control of Active Structures*. Springer Netherlands, 2011.

[9] Shannon A Rios and Andrew J Fleming. A new electrical configuration for improving the range of piezoelectric bimorph benders. *Sensors and Actuators A: Physical*, 224:106–110, 2015.

[10] Y Chida, T Nishimura, and Y Oguri. Piezoelectric bending actuator, March 14 1989. US Patent 4,812,698.

[11] Q M Wang and L E Cross. Performance analysis of piezoelectric cantilever bending actuators. *Ferroelectrics*, 215(1):187–213, 1998.

[12] S R Anton and H A Sodano. A review of power harvesting using piezoelectric materials (2003–2006). *Smart materials and Structures*, 16(3):R1, 2007.

[13] C A Randall, A Kelnberger, G Y Yang, R E Eitel, and T R Shrout. High strain piezoelectric multilayer actuators—a material science and engineering challenge. *Journal of electroceramics*, 14(3):177–191, 2005.

[14] Yuen Kuan Yong, Bharath Bhikkaji, and SO Reza Reza Moheimani. Design, modeling, and fpaa-based control of a high-speed atomic force microscope nanopositioner. *IEEE/ASME Transactions on Mechatronics*, 18(3):1060–1071, 2013.

[15] B P Baillargeon and S S Vel. Active vibration suppression of sandwich beams using piezoelectric shear actuators: experiments and numerical simulations. *Journal of Intelligent Material Systems and Structures*, 16(6):517–530, 2005.

[16] Q M Zhang, H Wang, and L E Cross. Piezoelectric tubes and tubular composites for actuator and sensor applications. *Journal of materials science*, 28(14):3962–3968, 1993.

[17] T G King, M E Preston, B J M Murphy, and D S Cannell. Piezoelectric ceramic actuators: A review of machinery applications. *Precision Engineering*, 12(3):131–136, 1990.

[18] C D Near. Piezoelectric actuator technology. In *Smart Structures and Materials 1996: Smart Structures and Integrated Systems*, volume 2717, pages 246–259. International Society for Optics and Photonics, 1996.

[19] N Jalili and K Laxminarayana. A review of atomic force microscopy imaging systems: application to molecular metrology and biological sciences. *Mechatronics*, 14(8):907–945, 2004.

[20] Y K Yong, S S Aphale, and S O R Moheimani. Design, identification, and control of a flexure-based xy stage for fast nanoscale positioning. *IEEE Transactions on Nanotechnology*, 8(1):46–54, 2009.

[21] Y K Yong, S O R Moheimani, B J Kenton, and K K Leang. Invited review article: High-speed flexure-guided nanopositioning: Mechanical design and control issues. *Review of scientific instruments*, 83(12):121101, 2012.

[22] G Schitter, P J Thurner, and P K Hansma. Design and input-shaping control of a novel scanner for high-speed atomic force microscopy. *Mechatronics*, 18(5):282–288, 2008.

[23] K K Leang and A J Fleming. High-speed serial-kinematic spm scanner: design and drive considerations. *Asian journal of control*, 11(2):144–153, 2009.

[24] L Liu, L Wu, J Sun, E Lin, and H Xie. Miniature endoscopic optical coherence tomography probe employing a two-axis microelectromechanical scanning mirror with through-silicon vias. *Journal of biomedical optics*, 16(2):026006–026006, 2011.

[25] A M Hess, D R Ibrahim, S R Lewis, J Venkataraghavan, and S Lakhapati. Fuel injector having piezoelectric actuator with preload control element and method, May 11 2010. US Patent 7,714,483.

[26] G Binnig, H Rohrer, C Gerber, and E Weibel. Surface studies by scanning tunneling microscopy. *Physical review letters*, 49(1):57, 1982.

[27] G Binnig and D P E Smith. Single-tube three-dimensional scanner for scanning tunneling microscopy. *Review of Scientific Instruments*, 57(8):1688–1689, 1986.

[28] Y K Yong, B Ahmed, and S O R Moheimani. Atomic force microscopy with a 12-electrode piezoelectric tube scanner. *Review of Scientific Instruments*, 81(3):033701, 2010.

[29] S O R Moheimani and Y K Yong. Simultaneous sensing and actuation with a piezoelectric tube scanner. *Review of Scientific Instruments*, 79(7):073702, 2008.

[30] G Binnig, C F Quate, and C Gerber. Atomic force microscope. *Physical review letters*, 56(9):930, 1986.

[31] R W Carpick and M Salmeron. Scratching the surface: fundamental investigations of tribology with atomic force microscopy. *Chemical reviews*, 97(4):1163–1194, 1997.

[32] R Garcia, A W Knoll, and E Riedo. Advanced scanning probe lithography. *Nature nanotechnology*, 9(8):577, 2014.

[33] X Liu, C Carbonell, and A B Braunschweig. Towards scanning probe lithography-based 4d nanoprinting by advancing surface chemistry, nanopatterning strategies, and characterization protocols. *Chemical Society Reviews*, 45(22):6289–6310, 2016.

[34] A A Tseng, A Notargiacomo, and T P Chen. Nanofabrication by scanning probe microscope lithography: A review. *Journal of Vacuum Science & Technology B: Microelectronics and Nanometer Structures Processing, Measurement, and Phenomena*, 23(3):877–894, 2005.

[35] B D Gates, Q Xu, J C Love, D B Wolfe, and G M Whitesides. Unconventional nanofabrication. *Annu. Rev. Mater. Res.*, 34:339–372, 2004.

[36] X Li, D MacDonald, and M Myaing. Scanning fiber-optic nonlinear optical imaging and spectroscopy endoscope, September 13 2007. US Patent App. 11/623,974.

[37] S Vilches, S Kretschmer, C Ataman, and H Zappe. Miniaturized fourier-plane fiber scanner for oct endoscopy. *Journal of Micromechanics and Microengineering*, 27(10):105015, 2017.

[38] S Vilches, S Kretschmer, C Ataman, and H Zappe. Forward-looking oct endomicroscope based on a compact fourier-plane piezo fiber scanner. In *Optical MEMS and Nanophotonics (OMN), 2017 International Conference on*, pages 1–2. IEEE, 2017.

[39] R Khayatzadeh, F Çivitci, and O Ferhanoğlu. Optimization of piezo-fiber scanning architecture for low voltage/high displacement operation. *Sensors and Actuators A: Physical*, 255:21–27, 2017.

[40] S Kuiper and G Schitter. Active damping of a piezoelectric tube scanner using self-sensing piezo actuation. *Mechatronics*, 20(6):656–665, 2010.

[41] G E Poirier. Atomic force microscope using piezoelectric detection, November 12 1996. US Patent 5,574,278.

[42] M Hannss, W Naumann, and R Anton. Performance of a tilt-compensating tube scanner in atomic force microscopy. *Scanning*, 20(7):501–507, 1998.

[43] Md Sohel Rana, Hemanshu R Pota, and Ian R Petersen. A survey of methods used to control piezoelectric tube scanners in high-speed afm imaging. *Asian Journal of Control*, 2018.

[44] W S Bacsa. Optical interference near surfaces and its application in subwavelength microscopy. In *Advances in Imaging and Electron Physics*, volume 163, pages 1–32. Elsevier, 2010.

[45] Chen and C Julian. Electromechanical deflections of piezoelectric tubes with quartered electrodes. *Applied Physics Letters*, 60(1):132–134, 1992.

[46] D G Fertis. *Nonlinear structural engineering: with unique theories and methods to solve effectively complex nonlinear problems*. Springer Science & Business Media, 2007.

[47] A J Fleming and Y K Yong. An ultrathin monolithic XY nanopositioning stage constructed from a single sheet of piezoelectric material. *IEEE/ASME Transactions on Mechatronics*, 22(6):2611–2618, Dec 2017.

[48] J N Reddy. *Energy Principles and Variational Methods in Applied Mechanics*. John Wiley & Sons, 2002.

[49] M L Bittencourt. *Computational Solid Mechanics: Variational Formulation and High Order Approximation*. CRC Press, 2014.

[50] C Y K Chee, L Tong, and G P Steven. A mixed model for composite beams with piezoelectric actuators and sensors. *Smart Materials and Structures*, 8(3):417, 1999.

[51] V Piefort. *Finite Element Modelling of Piezoelectric Active Structures*. PhD thesis, 2001.

[52] H F Tiersten. Hamilton's principle for linear piezoelectric media. *Proceedings of the IEEE*, 55(8):1523–1524, Aug 1967.

[53] S M Han, H Benaroya, and T Wei. Dynamics of transversely vibrating beams using four engineering theories. *Journal of Sound and Vibration*, 225(5):935–988, 1999.

[54] A Benjeddou. Advances in piezoelectric finite element modeling of adaptive structural elements: a survey. *Computers & Structures*, 76(1–3):347–363, 2000.

[55] L Meirovitch. *Fundamentals of Vibrations*. McGraw Hill, 2000.